Spatial distribution of tracers for optical sensing of stream surface flow

Alonso Pizarro[1], Silvano F. Dal Sasso[1], Matthew Perks[2], Salvatore Manfreda[3]

[1]Department of European and Mediterranean Cultures, University of Basilicata, Matera, 75100, Italy
5 [2]School of Geography, Politics and Sociology, Newcastle University, Newcastle-upon-Tyne, NE1 7RU, UK
[3]Department of Civil, Architectural and Environmental Engineering, University of Naples Federico II, Naples, 80125, Italy

Correspondence to: Alonso Pizarro (alonso.pizarro@unibas.it)

Abstract. River monitoring is of particular interest for our society that is facing increasing complexity in water management. Emerging technologies have contributed to opening new avenues for improving our monitoring capabilities, but also generating

10 new challenges for the harmonised use of devices and algorithms. In this context, optical sensing techniques for stream surface flow velocities are strongly influenced by tracer characteristics such as seeding density and level of aggregation. Therefore, a requirement is the identification of how these properties affect the accuracy of such methods. To this aim, numerical simulations were performed to consider different levels of particle aggregation, particle colour (in terms of greyscale intensity), seeding density, and background noise. Two widely used image-velocimetry algorithms were adopted: i) Particle Tracking

15 Velocimetry (PTV), and ii) Large-Scale Particle Image Velocimetry (LSPIV). A descriptor of the seeding characteristics (based on density and aggregation) was introduced based on a newly developed metric π. This value can be approximated and used in practice as $\pi = \nu^{0.1} / \left(\frac{\rho}{\rho_{cv1}} \right)$ where $\nu, \rho,$ and ρ_{cv1} are the aggregation level, the seeding density, and the converging seeding density at $\nu = 1$, respectively. A reduction of image-velocimetry errors was systematically observed by decreasing the values of π; and therefore, the optimal frame window was defined as the one that minimises π. In addition to numerical

20 analyses, the Basento field case study (located in southern Italy) was considered as a proof-of-concept of the proposed framework. Field results corroborated numerical findings, and an error reduction of about 15.9 and 16.1% was calculated - using PTV and PIV, respectively - by employing the optimal frame window.

1 Introduction

River streamflow observations are of enormous importance for environmental protection and engineering practice in general

25 (Anderson et al., 2006; Manfreda, 2018; Manfreda et al., 2020; Owe, 1985). Such observations are critical for any hydrological and hydraulic applications. In turn, it enables the understanding of more complex processes such as flash flood dynamics (Perks et al., 2016), the interaction of fish upstream and downstream of dams (Strelnikova et al., 2020), sediment transport dynamics (Batalla and Vericat, 2009), and bridge scour (Manfreda et al., 2018a; Pizarro et al., 2017).

Streamflow measurement campaigns are generally expensive and time-consuming, requiring the presence of high-qualified

30   personnel and forward planning (Tauro et al., 2018). Such approaches are typically based on pointwise measurements performed with flowmeters or acoustic doppler current profilers (ADCPs) that require the direct access of the operators or devices into the water. On the one hand, this is necessary to provide a full description of the flow velocity profile, but on the other hand, it may alter the measurements given the potential interaction of these elements with the flux. This issue has been partially dealt with by the use of non-contact approaches, as a timely alternative for river flow monitoring. Progress in the

35   development of non-contact approaches (such as image velocimetry, radars, and microwave systems) has been promising in recent years, opening the possibility for real-time, non-contact, flow monitoring. In particular, the advancements of image processing techniques have led to improvements of image-based approaches for surface flow velocity (SFV) estimation and this has enhanced the range of potential applications. Several techniques, such as Particle Tracking Velocimetry (PTV) and Large-Scale Image Velocimetry (LSPIV), have been proposed and applied in field campaigns to accurately estimate SFV from

40   video acquisitions (Bechle et al., 2012; Huang et al., 2018; Tauro and Salvatori, 2017). In turn, videos can be recorded from different devices (fixed-station located close to the river-section of interest, using cell phones or onboard Unmanned Aerial Systems (UASs)), allowing an easy and portable way to estimate SFVs and, consequently, river discharge (Leitão et al., 2018; Manfreda et al., 2018b; Pearce et al., 2020; Perks et al., 2016; Tauro et al., 2015).

The PTV technique revolves around particle identification and tracking (Lloyd et al., 1995) that can be implemented through

45   cross-correlation (Brevis et al., 2011; Lloyd et al., 1995), relaxation (Wu and Pairman, 1995), among other methods. Additionally, particle trajectories can be reconstructed, adding valuable information to the analysis and making it possible to apply trajectory-based filters to ensure realistic trajectories (Eltner et al., 2020; Tauro et al., 2019). On the other side, LSPIV techniques apply Particle Image Velocimetry (PIV) principles (Adrian, 1991, 2005; Peterson et al., 2008; Raffel et al., 2018) to large scales and natural environments (Fujita et al., 1998). Interesting to mention, LSPIV recognises and tracks patterns

50   instead of single tracers, while PTV single tracers.

These techniques are widely used, but it is hard to quantify their accuracy at field scales. This can be influenced by: i) environmental conditions, which can both deteriorate and enhance the image quality during the acquisition period (Le Coz et al., 2010; Muste et al., 2008); and ii) the characteristics of the tracers/features, such as colour, dimension, shape, seeding density, and aggregation level (Dal Sasso et al., 2018, 2020; Raffel et al., 2018). PTV and LSPIV need features to identify,

55   match and track to compute surface flow velocities. High seeding densities are, however, rare in natural environments and as a consequence, a general practice is the use of artificial tracers to increase the surface seeding in the field of view (Dal Sasso et al., 2018; Tauro et al., 2014, 2017). In this context, Figure 1 shows three different real case-study examples of natural and artificial seedings that tend to cluster. Remarkably, Figure 1.A reports high seeding aggregation levels and complex cluster structures during a flood event at the Tiber river in Italy (Tauro et al., 2017), whereas Figure 1.B and 1.C present the case when

60   artificial seeding is introduced in the river system for image-velocimetry analysis (Detert et al., 2017; Tauro et al., 2017). More information about the mentioned case studies can be found elsewhere (Perks et al., 2019).
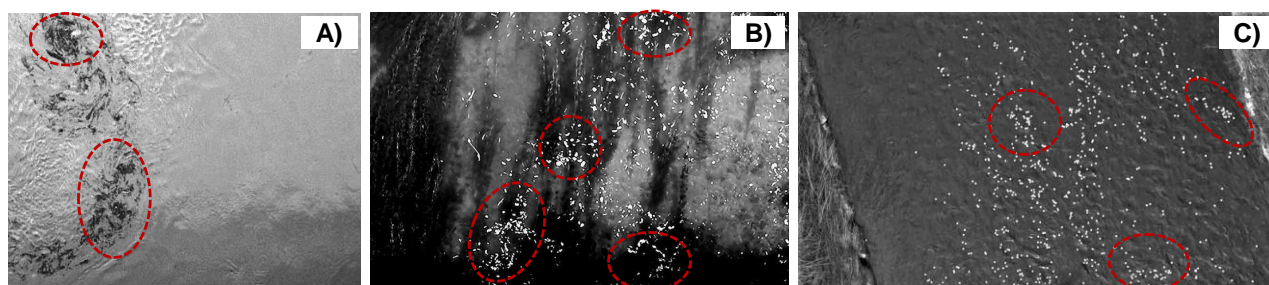
Figure. 1. Examples of moving and aggregated structures on the water surface: A) Natural seeding during a flood event at the Tiber river, Italy (Tauro et al., 2017); B) and C) Artificial seeding at low/intermediate flow conditions at Brenta river in Italy (Tauro et al., 2017) and Murg river in Switzerland (Detert et al., 2017), respectively.

The spatial distribution of artificial tracers is, however, operator-dependent and influenced by their experience, the type of material deployed, and amount. External environmental and river conditions such as wind and turbulence are also important factors. This issue is extremely relevant for discharge estimates recovered through image-based approaches since velocity errors are transmitted to streamflow estimations. In consequence, and even by using up-to-date approaches, monitoring complex flows, and extreme flood events, is still a challenge.

This paper aims to quantify the accuracy of SFV estimates under different seeding densities and aggregation levels. To achieve this, the following objectives were proposed: i) generation of numerical simulations of synthetically aggregated tracers to produce 33,600 synthetic images of known seeding characteristics; ii) using these synthetic images, a functional relationship between seeding densities, aggregations levels, and image velocimetry errors was derived under controlled conditions; iii) analysis was undertaken on footage acquired of the Basento River to determine how variations in seeding characteristics such as seeding density and aggregation level influence the image velocimetry errors in an uncontrolled field environment. Finally, iv) the function developed in ii) was applied to the Basento River to enable the selection of the optimal image frame sequence to minimise relative errors.

The rest of the paper is organised as follows: Section 2 presents the numerical framework for synthetic image generation; a description of the hydrological characteristics of the Basento case study, which is used as a proof-of-concept and; an outline of the PTV and PIV techniques adopted in analysis. Section 3 analyses the effects of seeding density and aggregation level on image-velocimetry results, using the synthetically generated images, and those of the Basento field case study. Conclusions at the end.

2 Methods

2.1 Numerical Simulations

Numerical simulations were performed to test two different image-velocimetry algorithms under controlled conditions, minimising the effects of external disturbances. In particular, the influence of tracer/feature properties on the final errors were

quantified. Synthetic tracers were randomly distributed in space with a unidirectional and constant velocity. They consist of uniform circular shapes with diameter Dxp ≈ 10 pixels (px) and uniform white colour. Both diameters and colours were altered

90   with white noise in order to consider more realistic configurations. Their spatial distribution was controlled by a Generalised Poisson Distribution (GPD) with a theoretical seeding density λ and level of aggregation υ.

The GPD was first introduced by Efron (1986), allowing the possibility to obtain point events randomly distributed in space with a given variance. The GPD has been used to model randomly distributed events in different studies (for instance, Good, Rodriguez-Iturbe, and Caylor (2013) and Manfreda, Caylor, and Good (2017) used the GPD to describe the spatial

95   characteristics of the landscape and vegetation organisation across climatological gradients). In this manuscript, the synthetic tracers are assumed to be randomly distributed in space with a mean number λS where S is the considered area. In consequence, the probability mass function that the random number of synthetic tracers, N, will be equal to a number n_i is given by Eq. (1),

$$f_{GPD(\lambda S)}(n_i) = \frac{1}{C_{GPD}} \frac{\exp\left(-\frac{\lambda S}{\upsilon}\right)}{\sqrt{\upsilon}} \left(\frac{\exp(-n_i)\, n_i^{n_i}}{n_i!}\right) \left(\frac{\exp(1)\, \lambda}{n_i}\right)^{n_i/\upsilon},$$ (1)

where λS and υ determine the location and the shape of $f_{GPD(\lambda S)}(n_i)$, and C_{GPD} is an integration constant.

Tracers moved with a constant velocity of 15 (px/frame) along the y-axis and within a grid of 500x500 pixels on a clear

100 background as representative of actual environmental conditions. Tracer diameter was set larger than 2.5 pixels in order to avoid peak locking effects (Cardwell et al., 2011; Dal Sasso et al., 2018; Nobach et al., 2005). Typical tracer dimensions at laboratory and field scales motivated the choice of Dxp ≈10 (px) for image-velocimetry experiments (Tauro et al., 2016).

Synthetic image sequences were generated varying the number of tracers in the spatial domain, allowing the consideration of 14 different seeding densities ranging from 0.4E-05 particles per pixel (ppp) up to 1.0E-02 (ppp). The range of variability was

105 established based on the typical values adopted in field surveys (Tauro and Grimaldi, 2017) and numerical studies (Dal Sasso et al., 2018). Tracer colour (in terms of greyscale intensity) and diameter were altered (introducing a Gaussian white noise with standard deviation equal to 0.05 and 0.3, respectively) to simulate environmental signal noises (possible changes in luminosity, brightness, and shadows). Figure 2 shows an example of synthetic image generations with different levels of aggregation and a fixed value of seeding density. In particular, the spatial distribution of tracers moves from an over-dispersed

110 organisation ($\upsilon = 0.5$), through a Poisson random distribution ($\upsilon = 1$) and an under-dispersed one ($\upsilon = 100$), to a super under-dispersed distribution ($\upsilon = 200$). Figure 2 (A, B, C and D) presents the original synthetic generation on the clear water background, while Figure 2 (E, F, G and H) shows the pre-processed images, enhancing the contrast between tracers and background (See Section 2.3). Furthermore, each numerical experiment contains 20 images, and each configuration was run 10 times. υ ranges from 0.5 to 200 (12 different values), and in consequence, 33,600 synthetic images were generated (14

115 different λ, 12 different υ, 20 images per configuration, and 10 times each configuration).
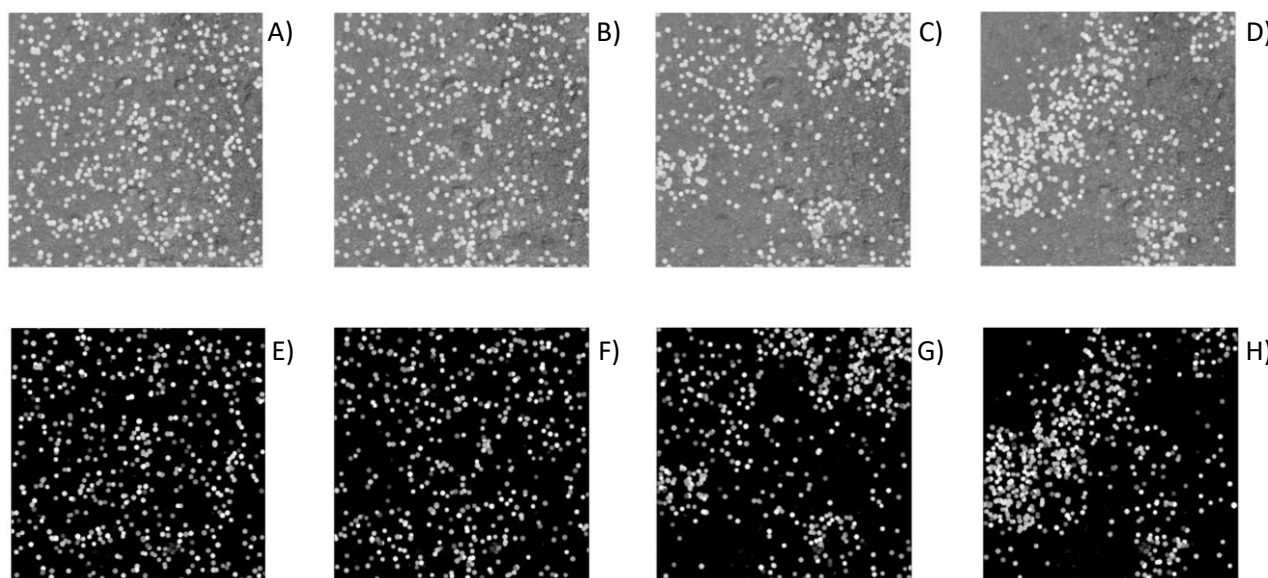
Figure. 2. Synthetic generations of spatial distribution of tracers assuming different values of the aggregation parameter ν = 0.5 (over-dispersed distribution - Fig 2.A, E), 1.0 (Poisson random distribution - Fig 2.B, F), 100 (under-dispersed distribution - Fig 2.C, G), and 200 (super under-dispersed distribution - Fig 2.D, H). Fixed value of the seeding density λ = 2.02E-03. The generation was carried out adopting a background in the images to provide more realistic conditions (A, B, C, D). Thereafter, images have been pre-processed to increase the contrast and better visualise tracers (E, F, G, H).

2.2 Proof-of-concept: The Basento case study

A field survey on the Basento River (Basilicata region, southern Italy) was carried out to test the outcomes of numerical simulations under real natural conditions. The cross-section considered for the measurements is located in the upper portion of the basin (catchment area of about 127 km^2) (Figure 3). The main river flow characteristics, at the moment of the video acquisition, were: i) river streamflow: 0.61 (m^3/s); ii) maximum flow depth: 0.38 (m); iii) river width: 6.0 (m); iv) maximum surface flow velocity: 0.68 (m/s); and, v) average surface flow velocity: 0.40 (m/s). Data were acquired using a DJI Phantom 3 Professional Quadcopter equipped with an integrated 4k UHD (ultra-high-definition) video recording camera and a 3-axis stabilised system. Video acquisition was performed using a Sony EXMOR 1/2.3" CMOS sensor and a greyscale video was captured from the UAS platform with a resolution of 1920x1080 (px) (i.e., FHD). The considered frame rate was set to 24 frames per second (fps). Reference objects, useful for image scale calibration and stabilisation, were positioned at visible locations on the riverbanks. The calibration factor converting pixels to meters was estimated, taking into consideration those objects with a known-a-priori dimension. The ground sampling distance (GSD) was, therefore, computed as 0.005 (m/px). Benchmark velocity measurements were performed using a current meter, in the proximity of the water-free surface, at 11 different locations across the river cross-section. The spanning distance between the respective measurements was 0.5 (m). Each measurement was made over a fixed acquisition period of 30 seconds. Artificial seeding was properly deployed onto the water surface, giving the possibility to create complex aggregated structures. Two operators were involved in the process, and artificial tracers made of wood chips were used to extra seed the region of interest (ROI).

The videos captured with the UAS were first stabilised using an automatic feature selection method that identifies features in
140 frame pairs, matching them to compute possible values of translation and rotation. The Features from Accelerated Segment
Test (FAST) detection algorithm was applied to identify features on an ad-hoc ROI. To improve the feature matching accuracy,
at each step, the method utilises the Random Sample Consensus (RANSAC) filter for unacceptable correspondences. The
application of the stabilisation algorithm has allowed the effects of camera movements to be reduced throughout the duration
of the video. Planimetric errors considering differences in translation and rotation were computed taking the first frame as the
145 reference target. On average, the reduction due to the stabilisation process goes from 64 to 7 (px) for the considered case study.
Therefore, movement in the original video is reduced by around 89%. The stabilisation algorithm does not require Ground
Control Points (GCPs) to be applied. Rather, it performs the detection of features automatically, and the stabilisation process
is, therefore, a good alternative for non-experienced users.

The Basento River presented low-flow conditions leading to subsampling the original video from 24 to 12 (fps). The choice
150 of the appropriate frame rate was made to ensure, on the one hand, a frame-by-frame displacement bigger than particle
dimension and, on the other hand, to minimise the effects of camera movement between frame pairs on the calculation of
surface velocity. As already mentioned, the footage was acquired in greyscale. A pre-processing procedure was applied using
the contrast stretching techniques to enhance the visibility of the artificial tracers against the background. For this purpose,
GIMP (the GNU Image Manipulation Program) was utilised to adjust brightness and contrast. This procedure eliminated a
155 large amount of noise caused by external reflections, improving the number of tracers identified and cross-correlation in the
ROI. Figure 3.B shows an example of the original frames (grayscale) and the pre-processed using GIMP (darker area
overlapping the original frame).
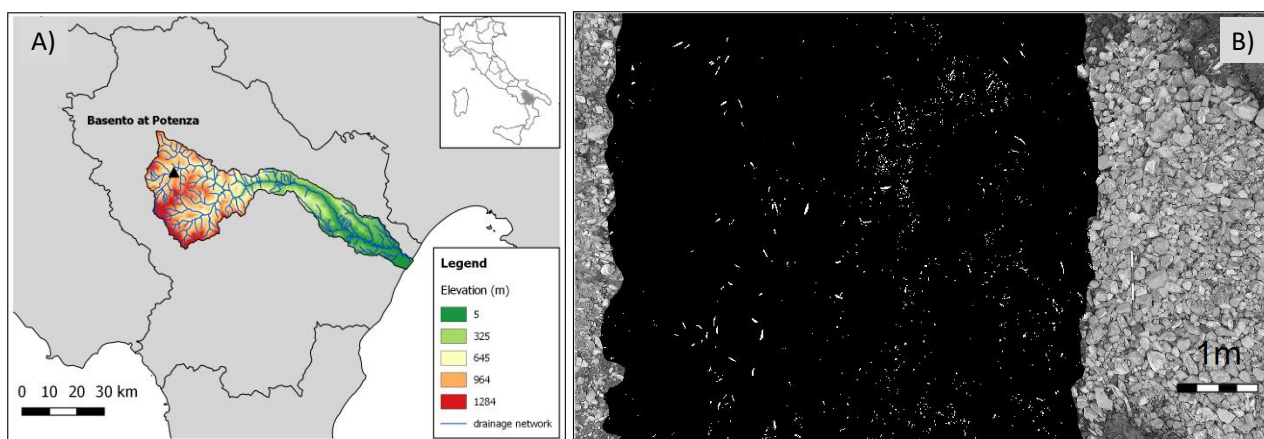
Figure. 3. A) Basento river and drainage basin with an indication of the measurement location (Basento at Potenza). B) Grayscale
160 **footage acquired with a DJI Phantom 3 Pro and corresponding footage after the pre-processing aimed at enhancing contrast for**
particle identification.

2.3 Image velocimetry analysis

PTV analyses were carried out employing a command-line version of PTVLab software (Brevis et al., 2011) that have been automated in order to handle the number of synthetic images. Tracer detection was performed using the particle Gaussian mask
165   correlation method (Ohmi and Li, 2000). Setting parameters in terms of particle diameter and reflectance intensity were set equal to 8 px and 70, respectively. Particle tracking was implemented using a cross-correlation algorithm (Wu and Pairman, 1995). The Interrogation Area (IA) was set at 20 px, cross-correlation threshold at 0.7, and neighbour similarity percentage at 25%. PIV analyses were performed employing a command-line version of PIVLab software (Thielicke and Stamhuis, 2014) written by the authors for the same purpose. The PIV algorithm was applied using the Fast Fourier Transform (FFT) with
170   three-passes standard correlation method (SA and IA sizes of 128x64, 64x32 and 32x16 px). Additionally, the 2x3-point Gaussian fit was employed to estimate the sub-pixel displacement peak. These setting parameters were carefully chosen to assure the right identification and tracking of synthetic tracers. For instance, PTV used a particle diameter of 8 px, while the synthetic diameter had an average value of 10 px with a standard deviation of 0.3 px. In addition, tracer movements must be inside the IA (PTV) and SA (PIV) for their right identification. The theoretical velocity was set at 15 px/frame, while IA and
175   SA were 20 and 32 px for PTV and PIV (minimum one of the three passes), respectively.
PTV parameter settings were slightly modified under field conditions due to the differences between the numerical and field datasets. In particular, the average tracer dimension at field conditions was estimated as 5 px and therefore, the particle diameter was set equal to 4 and the IA at 25 (px).
Finally, the quality of the results was determined by the magnitude of the errors that were computed as

$$\epsilon = 100 \times \frac{(u_c - u_R)}{u_R}, \tag{2}$$

180   where u_c is the computed velocity and u_R is the theoretical (numerical case) or measure (field case) velocity.

3 Results and Discussion

3.1 Numerical Analysis

The performance of PTV and PIV tracking algorithms was assessed by the calculation of errors (considering the imposed theoretical surface velocity) to test how the seeding density and aggregation level influence on the final velocity results. PTV
185   used 8 and 20 (px) for detection and tracking, respectively. PIV used FFT with three-passes (128x64, 64x32, 32x16). No post-processing method was applied to filter the spatiotemporal velocity results. The ROI was taken as the original dimension of the synthetic image generation, i.e. 500x500 (px). The processing times, considering the 33,600 synthetic generated images, for PIV and PTV analyses were 4,736 and 18,548 seconds, respectively. The same hardware (Processor i7-8700 CPU @ 3.20 GHz 3.19 GHz and RAM 32 GB) was used for both image-velocimetry analyses, leading to a fair comparison between them.

Hydrology and
Earth System
Sciences
Discussions

Open Access

EGU

190 PTV computing time was almost four times higher than PIV under the circumstances considered in this study. For all the cases, PTV and PIV techniques systematically underestimated the theoretical velocity independently of the seeding density and aggregation level under consideration. Consequently, only negative errors were observed with numerical results, in agreement with previously published work (Dal Sasso et al., 2018).

Figure 4 shows the PTV and PIV error results with different values of seeding densities and aggregation levels. A comparison

195 between PTV and PIV is shown in Figure 4.A, where each data point is associated with a colour that is scaled based on the theoretical seeding density adopted in the generation of synthetic images. A strong dependence between image-velocimetry results and seeding density was observed: errors can be reduced by increasing the seeding density. In all cases, PTV outperformed PIV under the synthetic conditions analysed in this study. These findings also support those of Tauro, Piscopia, and Grimaldi (2017) who found that PTV outperformed PIV in two different field case studies (Brenta and Tiber Rivers). It is

200 noteworthy that the obtained results refer to a single synthetic experiment that, although realistic, is not representative of any field condition. Therefore, further investigations with a larger set of idealised and field circumstances should be carried out to generalise the obtained results.
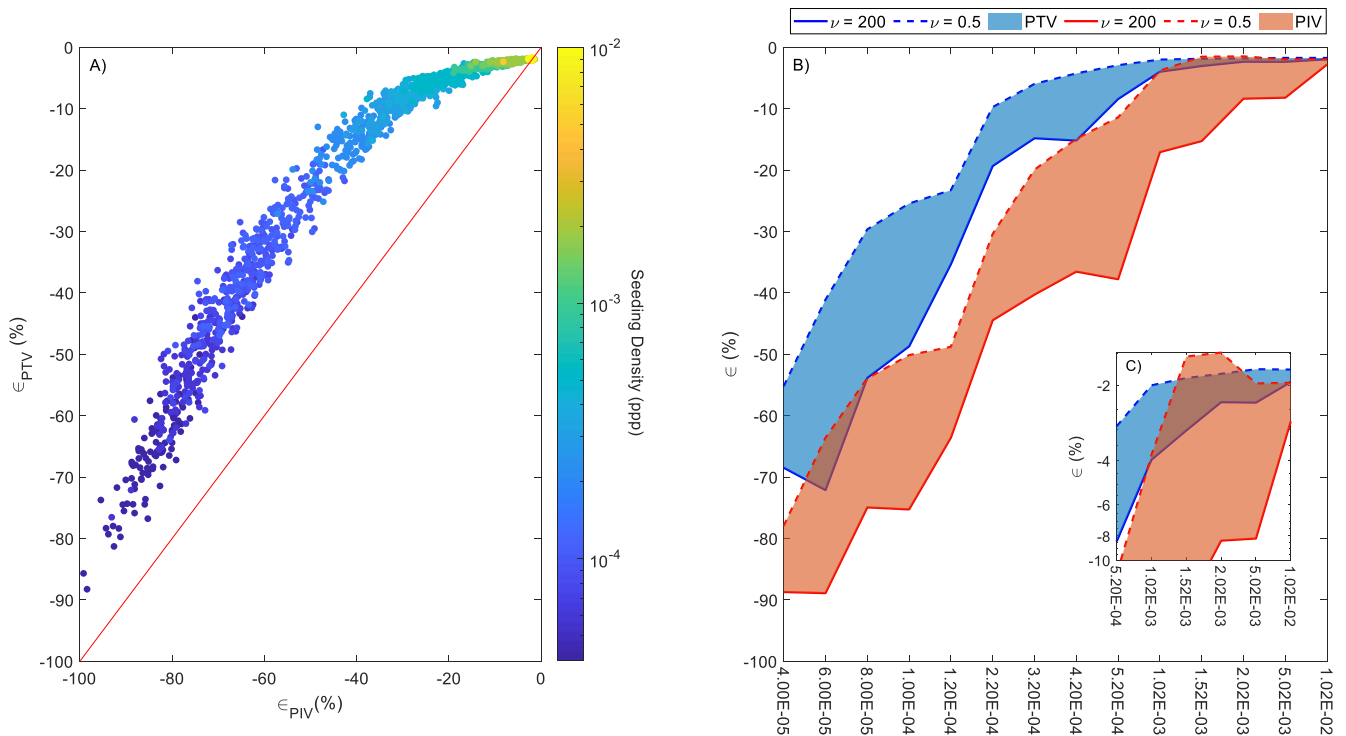
Figure 4. Comparison of PTV and PIV results using synthetic images with different values of seeding density and aggregation level.
205 **A) PTV vs PIV errors (ϵ_{PTV} and ϵ_{PIV}, respectively). Each data point is associated with a colour that is scaled based on the theoretical seeding density adopted in the numerical generation of synthetic images. B) Envelope error curves and areas in function of seeding density and level of aggregation ν. The blue and orange colours are associated with PTV and PIV results, respectively. Dashed and solid lines are associated with $\nu = 0.5$ and $\nu = 200$, respectively. C) Zoom of the right upper portion of B).**

Figure 4.B shows the envelope error curves (and areas between them) for a range of seeding densities and level of aggregation

210 ν. The blue and orange colours are associated with PTV and PIV error results, while dashed and solid lines are associated with ν = 0.5 and ν = 200, respectively. For the sake of simplicity, Figure 4.B only shows the extreme cases when ν = 0.5 and ν = 200; nevertheless, all the other cases (with ν values between these extreme considered cases) were confined and within these envelope curves. Error results of both techniques were influenced by ν, with a higher aggregation level tending to deteriorate the accuracy of image-velocimetry results, producing higher errors and associated variability across the range of seeding

215 densities. When the sensitivity of PIV and PTV to changes in ν are compared, it is clear that PIV is generally more sensitive than PTV, as demonstrated by the greater distance between ν = 0.5 and ν = 200 lines for a given seeding density, and by the orange shaded area being greater than the blue. The seeding density leading to the minimum converging error (around 2 – 3%) depended on ν. For instance, considering the PIV case, the converging seeding density values were 1.52E-03 and 1.02E-02 for ν = 0.5 and ν = 200, respectively. The converging seeding density values for PTV were 1.02E-03 and 2.02E-03 for ν = 0.5 and

220 ν = 200, respectively.

These numerical results are useful to visualise more-in-depth trends under controlled flow conditions, avoiding external disturbances. Results demonstrated that the minimum required seeding density to produce an error equal or lower than 3% differs slightly between the two techniques. We used this percentage as a reference error in order to derive a reference seeding density associated with a known error. It was observed that PIV required 1.52E-03 (ppp), while PTV needed about 1.02E-03

225 (ppp) to reach the same error. Notably, seeding densities lower than 1.0E-03 produced larger errors (larger than 3%) and consequently, flows should be extra-seeded in field campaigns for optimal implementation of the methods. This practice should always be adopted since typical natural flows are not characterised for presenting elevated transiting features, with maybe the exception of high flows. Furthermore, the effective seeding density (defined as the seeding that the algorithms are genuinely able to identify, match, and track) is always lower than the one transiting onto the water surface and therefore, the extra seed

230 practice is recommended. We are aware that this recommendation may not be practical in all conditions since fixed cameras can operate remotely without the necessity to be in-person at the field site. Furthermore, deploying material in wide channels or difficult-to-access areas can be challenging.

Following dimensional considerations, a model of the image-based errors can be formulated. Since the only variables considered in this study were the aggregation level and the seeding density, it is hypothesised that these errors depend on only

235 these variables. In functional form

$$f(\epsilon, \nu, \rho, \rho_{cv1}) = 0,\qquad(3)$$

where f = function, and ρ and ρ_{cv1} are the seeding density and the converging seeding density at $\nu = 1$ (Poisson case taken as a reference). According to the Buckingham-π theorem, Eq. (3) can be rewritten in terms of dimensionless parameters as follows

$$\epsilon = f\left(\nu, \frac{\rho}{\rho_{cv1}}\right). \tag{4}$$

The function f is usually considered as a multiplication of power laws. In this study, we partially follow this approach and

240 also hypothesise that the functional relationship f is described by a two-parameter exponential function:

$$\epsilon = c_1(1 - e^{-c_2\pi}), \tag{5}$$

where $\pi = \nu^{k_1}\left(\frac{\rho}{\rho_{cv1}}\right)^{k_2}$ is the multiplication of power laws; and, c_1, c_2, k_1, k_2 are fitting coefficients. Model performance was

quantified by means of the root mean square error (RMSE) and the Nash-Sutcliffe efficiency (NSE) for prediction of the

image-velocimetry errors. In turn, the fitting coefficients were calibrated using the MATLAB genetic algorithm optimising

RMSE. Table 1 summarises the results of the calibration process for both PTV and PIV, while Figure 5 shows the image-

245 velocimetry errors in function of π, and observed versus computed errors. It is observed from Eq. (5) and π can correctly

reproduced the main dynamics of the image-velocimetry errors, reporting low RMSE values in calibration (5.34 and 5.77%

for PIV and PTV, respectively). A visual inspection of Figure 5.A1 and 5.B1 shows that increasing π values leads to higher

errors for both image-velocimetry techniques. Figure 5.A2 and 5.B2 also show that the predictive capacity of Eq. (5) is higher

at low PTV and PIV error values.

250 Even though PIV and PTV work differently, the fitted values in Eq. (5) were similar. Remarkably, k_1 and k_2 showed that the

dimensionless π parameter can be approximated and used in practice as $\pi = \nu^{0.1}/\left(\frac{\rho}{\rho_{cv1}}\right)$. Furthermore, considering that the

errors are minimised when π takes low values, π can be used in field conditions as a descriptor to choose the optimal portion

of a video to analyse in order to minimise the errors in image-velocimetry estimates as a function of seeding density and

aggregation level. This novel idea is explored in the next subsection, taking the Basento River as a proof-of-concept case study.

255

Table 1. Calibrated values of c_1, c_2, k_1, k_2 and model performances in terms of RMSE (%) and NSE. PTV and PIV calibration results. ρ_{cv1} values for PIV and PTV were taken from Figure 4 and are 1.52E-03 and 1.02E-03, respectively.

|	c_1	c_2	k_1	k_2	RMSE (%)	NSE
PTV	-71.87	0.04	0.10	-1.09	5.77	0.92
PIV	-78.49	0.07	0.10	-1.06	5.34	0.97
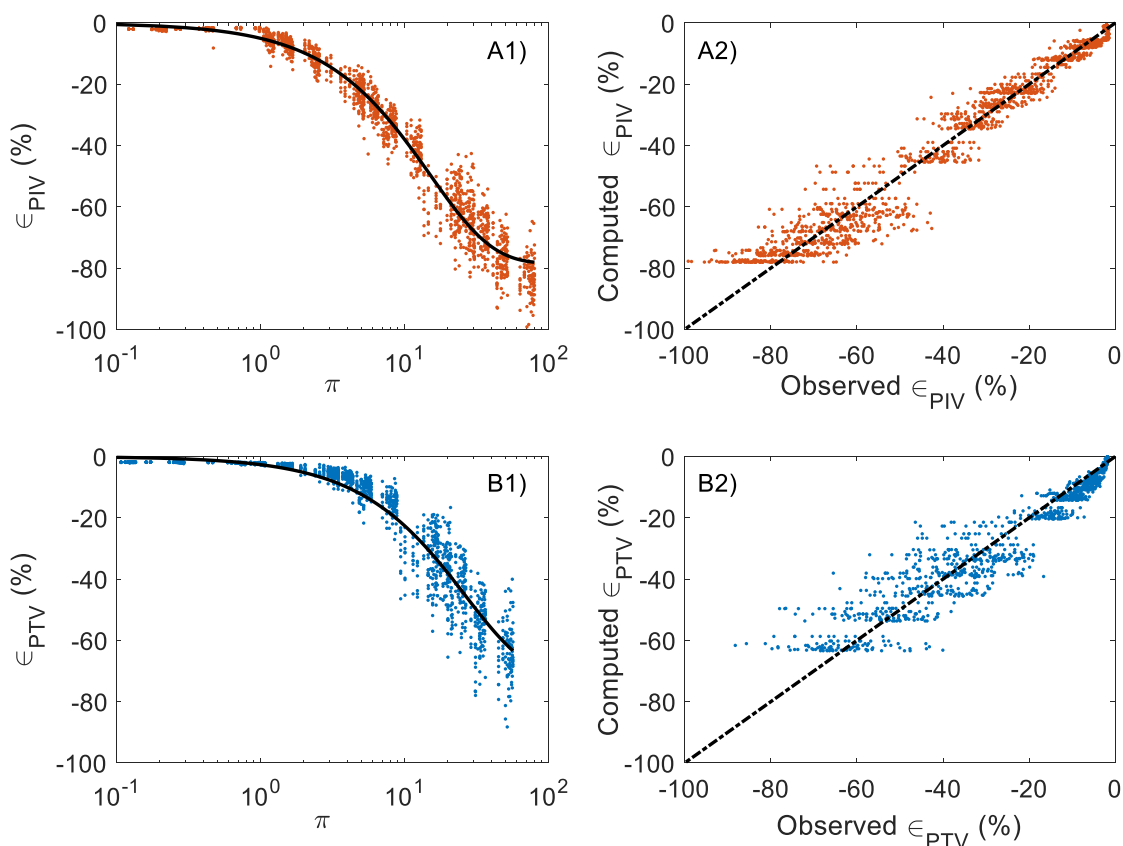
Figure 5. Image-velocimetry errors in function of π (A1 and B1) and observed versus computed errors (A2 and B2). Blue and orange colours are related to PTV and PIV numerical error results. Solid lines represent Eq. (5), while the dashed lines are the perfect agreement between observed and computed image-velocimetry errors.

3.2 Field Campaign: The Basento case study

Outcomes of the numerical analysis were tested on a real case study in order to identify the best temporal window for image velocimetry analyses. The case study was selected due to the spatial distribution of tracers varying significantly during the recording period, making it challenging to manually select the optimal frames for analysis. Figure 6 displays a pre-processed frame with the location of the measuring points using standard equipment (from L1 to L11). These surface flow velocity measurements were taken as reference velocities for PTV and PIV benchmarking. Figure 6.B and 6.C show a zoom of the ROI and the identification of transiting features, respectively. An example of identified features is presented in Figure 6.D. In this Figure, the number of features, their relative positions and associated areas were identified using an ad-hoc algorithm recently developed by the authors. This enables characterisation of the seeding properties (i.e., empirical seeding densities and aggregation levels) on a frame-by-frame basis even if shapes and dimensions of the tracers vary considerably. Using this approach, the empirical aggregation level (i.e., the empirical one equivalent to the used in the numerical simulations), was quantified through the dispersion index D. $D = \sigma^2/\mu$, where σ^2 and μ are the variance and mean values of the seeding density

11

275 computed in sub-patches of the same size. This metric is normally measured to quantify whether a set of events are clustered or dispersed. As in the numerical case, D = 1 means features follow a Poisson distribution, while D < 1 and D > 1 follow an over- and under-dispersed spatial distribution.
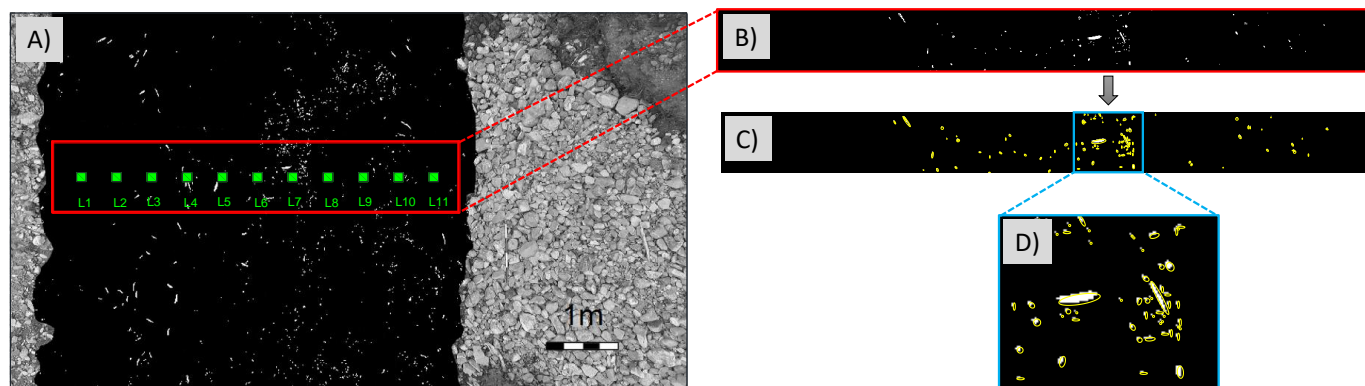
Figure 6. A) Pre-processed frame indicating the ROI and the reference measuring locations for benchmark purposes. The isolation
280 **of the ROI is presented in B), while in C) an example of identified features on the water surface. D) Zoom of an arbitrary portion of the ROI with the identified features.**

Figure 7 shows a comprehensive overview of the seeding behaviour during the 200 frames considered for the analysis. Figure 7.A and 7.B present the seeding density in ppp, and the dispersion index D computed as a function of the frame number. The minimum and maximum values for seeding density – and dispersion index – were 1.3E-04 and 2.9E-03 (ppp) – and 4.1 and

285 57.3 –, respectively. Additionally, the estimated mean area of features (computed frame-by-frame and inside the ROI) varied between 1.5 and 3.5 cm^2 approximately.
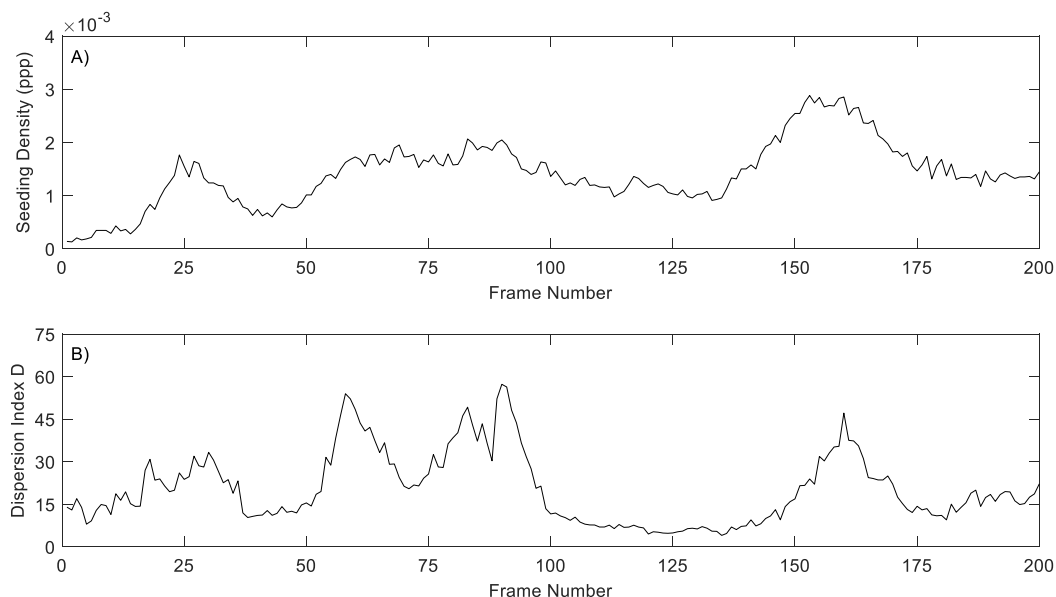

Figure 7. Overview of seeding characteristics on the ROI of the Basento River during the acquisition time: A) Seeding density in ppp, B) Dimensionless dispersion index D.

Hydrology and
Earth System
Sciences
Discussions

Open Access

EGU

290   The approach mentioned above made it possible to compute π and correctly identify the worst and best part of the video for

image velocimetry analysis. A moving window of 100 frames was arbitrarily chosen, on which an average dispersion index D

and seeding density was computed. This decision was motivated to increase the odds of populating the entire ROI with features.

The empirical π was then calculated as $\pi = \bar{D}^{0.1} / \left(\frac{\bar{\rho}}{\rho_{cv1}} \right)$, where $\bar{D}$ and $\bar{\rho}$ are the average-in-100-frames dispersion index and

seeding density, respectively. Figure 8.A depicts π in function of the frame windows. Triangle markers correspond with the

295   minimum and maximum value of π and their respective locations (82-181 and 1-100, respectively). Figure 8.A shows the

particular case of PTV; nevertheless, PIV presented similar results. The locations of the minimum and maximum π values was,

therefore, unaffected by the image-velocimetry technique under consideration.
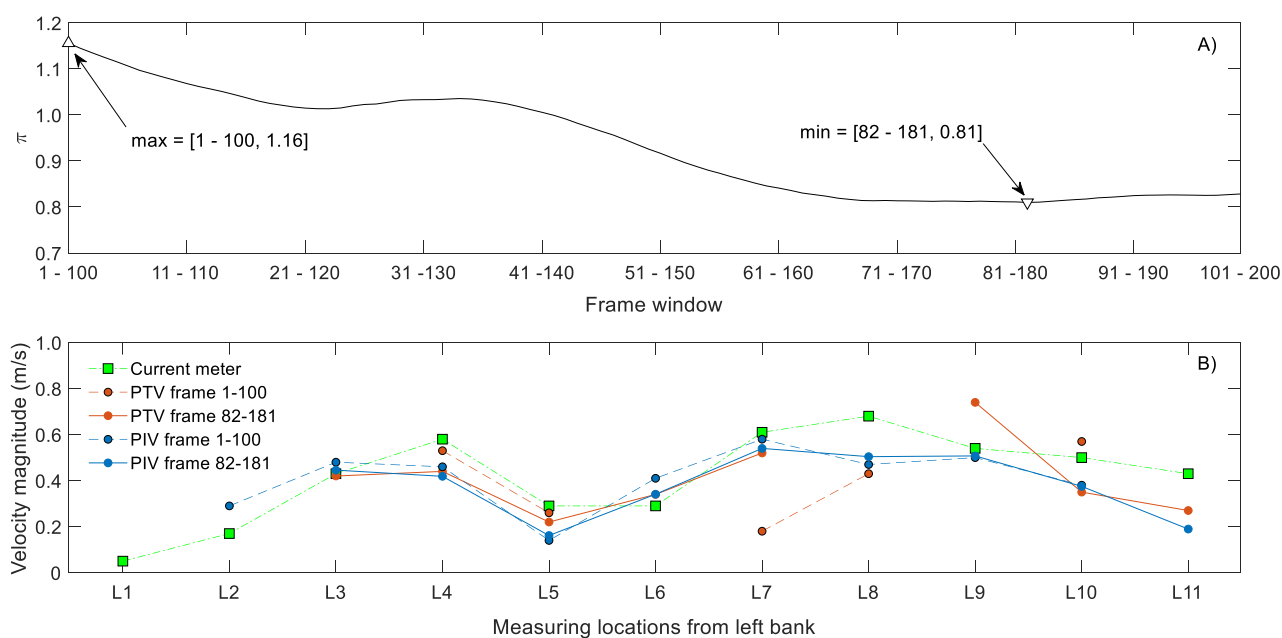
Figure 8. A) π in function of the frame windows considering 100 frames. Triangle markers correspond with the minimum and
300   **maximum value of π. Their locations were 82-181 and 1-100, respectively. Particular case of PTV, whereas PIV showed similar**
results and the locations of the minimum and maximum π values were unaffected by the image-velocimetry technique. B)
Comparison between PTV and PIV data for experiments on the Basento River. Values recorded with the current meter are also
reported for a rapid visual assessment (green squares). Blue and orange colours represent PTV and PIV data.

Image-based velocity results were averaged in a block of 30x30 cm^2 for a fair comparison among PTV, PIV, and benchmark

305   velocity values. The measuring locations corresponded with the centre of the blocks. Computed velocities across the cross-

section and reference velocities are reported in Figure 8.B. The blue and orange colours are associated with PTV and PIV

results, respectively (same colours used within numerical results for consistency and fast visual comparison). Green squares

are the velocities measured using the current meter. Notably, the measuring location L1 had no computed velocity values due

to the lack of features transiting on this part of the ROI, whereas only PIV was able to compute velocities at L2. This issue can

310   be explained due to the inherent property of PIV that is able to identify and track other features such as ripples and other

13

structures transiting on the water surface. Interestingly, and in agreement with numerical results, 80% (frames 1-100) and 75% (frames 82-182) of the computed velocity measuring locations underestimated the reference velocities using PTV. Similarly, results using PIV were 67 and 78%, respectively. Therefore, a close agreement was observed with the numerical results that systematically presented underestimations of computed velocities in comparison with the theoretical one. Interesting to

315 mention is also the fact that considering the optimal frame window allowed the computation of velocities over more reference locations than using frames 1 - 100 (PTV: 72.7 vs 45.5%; PIV: 81.8 vs 81.8%).

Both image-velocimetry approaches correctly captured the mean behaviour of velocities across the cross-section. Table 2 presents summarised information of the average-in-100-frames seeding density and dispersion index as well as the initial and final frame used for image-velocimetry purposes. The π value is also presented as well as the absolute average error across the

320 cross-section. As expected from numerical analyses, an error reduction of about 15.9% (PTV) and 16.1% (PIV) was found on the Basento case study by employing the optimal frame window that minimises π. It is therefore recommended that π is used as a descriptor of the optimal portion of a video to analyse.

325 **Table 2. Overview of features characteristics, minimum and maximum π values, and absolute errors using PTV and PIV. Values in parenthesis correspond with the error reduction using the optimal frame window.**

Frames (from – to)	$\overline{\rho}$ (ppp)	$\overline{D}$	π		Absolute average Error (%)		Absolute Error Eq. (5) (%)	
			PTV	PIV	PTV	PIV	PTV	PIV
1 - 100	1.2E-03	26.1	1.16	1.72	27.72	28.74	3.70	8.91
82 - 181	1.7E-03	18.2	0.81	1.21	23.31 (15.9)	24.11 (16.1)	2.61 (29.5)	6.36 (28.6)

Finally, considering numerical findings, field image-based estimates presented larger errors in comparison with numerical results for the respective same values of π (last two columns of Table 2). This is despite the average seeding density being relatively high (~1.5E-03) and the average dispersion index relatively low (~20). Possible reasons for deteriorations in PTV

330 and PIV estimates can be attributed to other variables such as video stabilisation issues, noise due to different environmental conditions (e.g., intermittent and different levels of illumination, water reflections, and presence of shadows), and different shapes and dimensions of features (stressing the matching and tracking process between consecutive frames). At this regard, Dal Sasso et al. (2020) recently introduced some metrics for the quantification of seeding characterisitics needed to enhance image-velocimetry performances in rivers. Among them, the seeding density, aggregation level, and coefficient of variation

335 of tracers' dimension were statistically significant to velocity estimation accuracy. These issues should be the subject of further investigation, along with the application of these ideas to case studies with very different field conditions to assess the uncertainty of computed surface velocities and remote river flow estimates.

4 Conclusions

In this paper, we investigated the performances of PTV and PIV for surface flow velocity estimations. Synthetic generation of

340   33,600 images was generated to test image-velocimetry techniques under different levels of tracer aggregation and seeding density. In all numerical cases, velocity results systematically underestimated the theoretical imposed velocity. A general trend was observed by increasing the seeding density and decreasing the level of aggregation, in which results were improved. The main advantage of the numerical proposed approach is the controlled conditions in which the analyses can be conducted, minimising the effects of external disturbances. This later helped to visualise the hidden trends that optimise image-based

345   estimates. Based on numerical findings, seeding densities lower than 1.0E-03 produced larger errors and in consequence, flows should be extra-seeded in field campaigns for optimal implementation of image velocimetry methods. Additionally, the dimensionless π parameter was introduced as a descriptor of the optimal portion of the video to analyse using the studied image-based techniques. Based on numerical results, π can be approximated and used in practice as $\pi = v^{0.1} / \left(\frac{\rho}{\rho_{cv1}} \right)$, where $v, \rho,$ and ρ_{cv1} are the aggregation level, the seeding density, and the converging seeding density at $v = 1$, respectively. A

350   reduction of image-based errors was observed by decreasing the values of π.

The Basento field case study (located in southern Italy) was considered as a proof-of-concept of the proposed framework. Seeding characteristics were empirically estimated through a novel algorithm recently developed by the authors, opening the possibilities of more refined analyses. The number of features, relative positions, and associated areas were saved for the computation of the empirical seeding densities and aggregation levels. The empirical π values were then computed, and two

355   extreme cases were considered for velocimetry comparison purposes: i) the one considering the maximum value of π (worst case), and ii) the one related to the minimum π (best case). Field results corroborated numerical findings, and an error reduction of about 15.9 and 16.1% was then calculated - using PTV and PIV, respectively - on the Basento case study by employing the optimal frame window. The optimal frame window was defined as the one that minimises π.

Interesting to note, field image-based estimates presented larger errors than numerical results for the respective same values

360   of π. Possible reasons deteriorating PTV and PIV estimates can be attributed to other variables such as: i) video stabilisation issues; ii) intermittent and different levels of illumination, water reflections, and presence of shadows; and, iii) different shapes and dimensions of features, stressing the matching and tracking process between consecutive frames. The authors are keen to apply these ideas to further assess the uncertainty in remote flow velocities and river discharge estimates.

References

Adrian, R.: Particle-Imaging Techniques For Experimental Fluid-Mechanics, Annu. Rev. Fluid Mech.,
doi:10.1146/annurev.fluid.23.1.261, 1991.

375 Adrian, R. J.: Twenty years of particle image velocimetry, Exp. Fluids, 39(2), 159–169, 2005.

Anderson, K. E., Paul, A. J., McCauley, E., Jackson, L. J., Post, J. R. and Nisbet, R. M.: Instream flow needs in streams and
rivers: The importance of understanding ecological dynamics, Front. Ecol. Environ., doi:10.1890/1540-
9295(2006)4[309:IFNISA]2.0.CO;2, 2006.

Batalla, R. J. and Vericat, D.: Hydrological and sediment transport dynamics of flushing flows: Implications for management
380 in large Mediterranean rivers, River Res. Appl., doi:10.1002/rra.1160, 2009.

Bechle, A., Wu Chin, H., Liu, W.-C. and Kimura, N.: Development and Application of an Automated River-Estuary Discharge
Imaging System, J. Hydraul. Eng., 138(4), 327–339, doi:10.1061/(ASCE)HY.1943-7900.0000521, 2012.

Brevis, W., Niño, Y. and Jirka, G. H.: Integrating cross-correlation and relaxation algorithms for particle tracking velocimetry,
Exp. Fluids, 50(1), 135–147, 2011.

385 Cardwell, N. D., Vlachos, P. P. and Thole, K. A.: A multi-parametric particle-pairing algorithm for particle tracking in single
and multiphase flows, Meas. Sci. Technol., 22(10), 105406, 2011.

Le Coz, J., Hauet, A., Pierrefeu, G., Dramais, G. and Camenen, B.: Performance of image-based velocimetry (LSPIV) applied
to flash-flood discharge measurements in Mediterranean rivers, J. Hydrol., 394(1), 42–52, 2010.

Dal Sasso, S. F., Pizarro, A., Samela, C., Mita, L. and Manfreda, S.: Exploring the optimal experimental setup for surface flow
390 velocity measurements using PTV, Environ. Monit. Assess., 190(8), doi:10.1007/s10661-018-6848-3, 2018.

Dal Sasso, S. F., Pizarro, A. and Manfreda, S.: Metrics for the quantification of seeding characteristics needed to enhance
image-velocimetry performances in rivers, Submitt. to Remote Sens., 2020.

Detert, M., Johnson, E. D. and Weitbrecht, V.: Proof-of-concept for low-cost and non-contact synoptic airborne river flow

measurements, Int. J. Remote Sens., doi:10.1080/01431161.2017.1294782, 2017.

395 Efron, B.: Double exponential families and their use in generalized linear regression, J. Am. Stat. Assoc., doi:10.1080/01621459.1986.10478327, 1986.

Eltner, A., Sardemann, H. and Grundmann, J.: Technical Note: Flow velocity and discharge measurement in rivers using terrestrial and unmanned-aerial-vehicle imagery, Hydrol. Earth Syst. Sci., 24(3), 1429–1445, doi:10.5194/hess-24-1429-2020, 2020.

400 Fujita, I., Muste, M. and Kruger, A.: Large-scale particle image velocimetry for flow analysis in hydraulic engineering applications, J. Hydraul. Res., 36(3), 397–414, 1998.

Good, S. P., Rodriguez-Iturbe, I. and Caylor, K. K.: Analytical expressions of variability in ecosystem structure and function obtained from threedimensional stochastic vegetation modelling, Proc. R. Soc. A Math. Phys. Eng. Sci., doi:10.1098/rspa.2013.0003, 2013.

405 Huang, W. C., Young, C. C. and Liu, W. C.: Application of an automated discharge imaging system and LSPIV during typhoon events in Taiwan, Water (Switzerland), doi:10.3390/w10030280, 2018.

Leitão, J. P., Peña-Haro, S., Lüthi, B., Scheidegger, A. and Moy de Vitry, M.: Urban overland runoff velocity measurement with consumer-grade surveillance cameras and surface structure image velocimetry, J. Hydrol., doi:10.1016/j.jhydrol.2018.09.001, 2018.

410 Lloyd, P. M., Stansby, P. K. and Ball, D. J.: Unsteady surface-velocity field measurement using particle tracking velocimetry, J. Hydraul. Res., 33(4), 519–534, 1995.

Manfreda, S.: On the derivation of flow rating curves in data-scarce environments, J. Hydrol., doi:10.1016/j.jhydrol.2018.04.058, 2018.

Manfreda, S., Caylor, K. K. and Good, S. P.: An ecohydrological framework to explain shifts in vegetation organization across 415 climatological gradients, Ecohydrology, doi:10.1002/eco.1809, 2017.

Manfreda, S., Link, O. and Pizarro, A.: A theoretically derived probability distribution of scour, Water (Switzerland), doi:10.3390/w10111520, 2018a.

Manfreda, S., McCabe, M. F., Miller, P. E., Lucas, R., Madrigal, V. P., Mallinis, G., Dor, E. Ben, Helman, D., Estes, L., Ciraolo, G., Müllerová, J., Tauro, F., de Lima, M. I., de Lima, J. L. M. P., Maltese, A., Frances, F., Caylor, K., Kohv, M., 420 Perks, M., Ruiz-Pérez, G., Su, Z., Vico, G. and Toth, B.: On the use of unmanned aerial systems for environmental monitoring, Remote Sens., doi:10.3390/rs10040641, 2018b.

Manfreda, S., Pizarro, A., Moramarco, T., Cimorelli, L., Pianese, D. and Barbetta, S.: Potential advantages of flow-area rating curves compared to classic stage-discharge-relations, J. Hydrol., 124752, 2020.

Muste, M., Fujita, I. and Hauet, A.: Large-scale particle image velocimetry for measurements in riverine environments, Water 425 Resour. Res., 44(4), 2008.

Nobach, H., Damaschke, N. and Tropea, C.: High-precision sub-pixel interpolation in particle image velocimetry image processing, Exp. Fluids, 39(2), 299–304, 2005.

Ohmi, K. and Li, H.-Y.: Particle-tracking velocimetry with new algorithms, Meas. Sci. Technol., 11(6), 603, 2000.

Owe, M.: Long-term streamflow observations in relation to basin development, J. Hydrol., 78(3–4), 243–260, 1985.

430 Pearce, S., Ljubičić, R., Peña-Haro, S., Perks, M., Tauro, F., Pizarro, A., Dal Sasso, S., Strelnikova, D., Grimaldi, S., Maddock, I., Paulus, G., Plavšić, J., Prodanović, D. and Manfreda, S.: An Evaluation of Image Velocimetry Techniques under Low Flow Conditions and High Seeding Densities Using Unmanned Aerial Systems, Remote Sens., doi:10.3390/rs12020232, 2020.

Perks, M., Sasso, S. F. D., Hauet, A., Coz, J. Le, Pearce, S., Peña-Haro, S., Tauro, F., Grimaldi, S., Hortobágyi, B., Jodeau, M., Maddock, I., Pénard, L. and Manfreda, S.: Towards harmonization of image velocimetry techniques for river surface 435 velocity observations, Earth Syst. Sci. Data Discuss., doi:10.5194/essd-2019-133, 2019.

Perks, M. T., Russell, A. J. and Large, A. R. G.: Technical note: Advances in flash flood monitoring using unmanned aerial vehicles (UAVs), Hydrol. Earth Syst. Sci., doi:10.5194/hess-20-4005-2016, 2016.

Peterson, S. D., Chuang, H. S. and Wereley, S. T.: Three-dimensional particle tracking using micro-particle image velocimetry hardware, Meas. Sci. Technol., doi:10.1088/0957-0233/19/11/115406, 2008.

440 Pizarro, A., Samela, C., Fiorentino, M., Link, O. and Manfreda, S.: BRISENT: An Entropy-Based Model for Bridge-Pier Scour Estimation under Complex Hydraulic Scenarios, Water, doi:10.3390/w9110889, 2017.

Pizarro, A., Silvano Fortunato, D. S., Perks, M. T. and Manfreda, S.: Data on spatial distribution of tracers for optical sensing of stream surface flow (Version 0.1), [Dataset] Zenodo, doi:10.5281/zenodo.3761859, 2020.

Raffel, M., Willert, C. E., Scarano, F., Kähler, C. J., Wereley, S. T. and Kompenhans, J.: Particle image velocimetry: a practical 445 guide, Springer., 2018.

Strelnikova, D., Paulus, G., Käfer, S., Anders, K.-H., Mayr, P., Mader, H., Scherling, U. and Schneeberger, R.: Drone-Based Optical Measurements of Heterogeneous Surface Velocity Fields around Fish Passages at Hydropower Dams, Remote Sens., doi:10.3390/rs12030384, 2020.

Tauro, F. and Grimaldi, S.: Ice dices for monitoring stream surface velocity, J. Hydro-environment Res., 14, 143–149, 2017.

450 Tauro, F. and Salvatori, S.: Surface flows from images: ten days of observations from the Tiber River gauge-cam station, Hydrol. Res., 48(3), 646–655, 2017.

Tauro, F., Porfiri, M. and Grimaldi, S.: Orienting the camera and firing lasers to enhance large scale particle image velocimetry for streamflow monitoring, Water Resour. Res., 50(9), 7470–7483, 2014.

Tauro, F., Pagano, C., Phamduy, P., Grimaldi, S. and Porfiri, M.: Large-scale particle image velocimetry from an unmanned 455 aerial vehicle, IEEE/ASME Trans. Mechatronics, 20(6), 3269–3275, 2015.

Tauro, F., Petroselli, A., Porfiri, M., Giandomenico, L., Bernardi, G., Mele, F., Spina, D. and Grimaldi, S.: A novel permanent gauge-cam station for surface-flow observations on the Tiber River, Geosci. Instrumentation, Methods Data Syst., 5(1), 241–251, 2016.

Tauro, F., Piscopia, R. and Grimaldi, S.: Streamflow Observations From Cameras: Large-Scale Particle Image Velocimetry or 460 Particle Tracking Velocimetry?, Water Resour. Res., 53(12), 10374–10394, 2017.

Tauro, F., Selker, J., Van De Giesen, N., Abrate, T., Uijlenhoet, R., Porfiri, M., Manfreda, S., Caylor, K., Moramarco, T.,

Benveniste, J., Ciraolo, G., Estes, L., Domeneghetti, A., Perks, M. T., Corbari, C., Rabiei, E., Ravazzani, G., Bogena, H., Harfouche, A., Broccai, L., Maltese, A., Wickert, A., Tarpanelli, A., Good, S., Lopez Alcala, J. M., Petroselli, A., Cudennec, C., Blume, T., Hut, R. and Grimaldia, S.: Measurements and observations in the XXI century (MOXXI): Innovation and multi-

465   disciplinarity to sense the hydrological cycle, Hydrol. Sci. J., doi:10.1080/02626667.2017.1420191, 2018.

Tauro, F., Piscopia, R. and Grimaldi, S.: PTV-Stream: A simplified particle tracking velocimetry framework for stream surface flow monitoring, Catena, doi:10.1016/j.catena.2018.09.009, 2019.

Thielicke, W. and Stamhuis, E. J.: PIVlab – Towards User-friendly, Affordable and Accurate Digital Particle Image Velocimetry in MATLAB, J. Open Res. Softw., doi:10.5334/jors.bl, 2014.

470   Wu, Q. X. and Pairman, D.: A relaxation labeling technique for computing sea surface velocities from sea surface temperature, IEEE Trans. Geosci. Remote Sens., 33(1), 216–220, 1995.